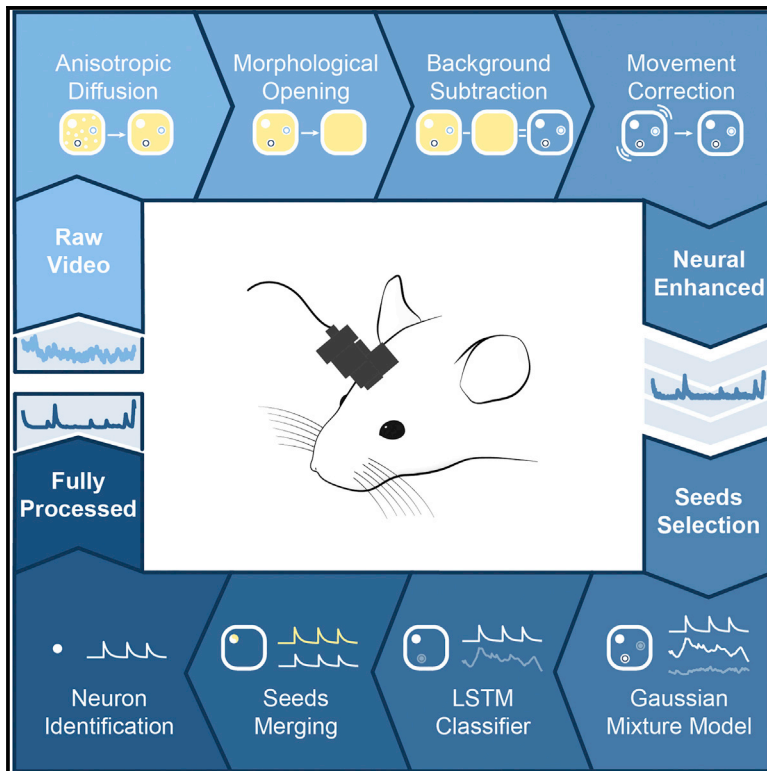


MIN1PIPE: A Miniscope 1-Photon-Based Calcium Imaging Signal Extraction Pipeline

Graphical Abstract



Authors

Jinghao Lu, Chunyuan Li, Jonnathan Singh-Alvarado, Zhe Charles Zhou, Flavio Fröhlich, Richard Mooney, Fan Wang

Correspondence

jinghao.lu@duke.edu (J.L.),
chunyuan.li@duke.edu (C.L.),
fan.wang@duke.edu (F.W.)

In Brief

Lu et al. develop an end-to-end pipeline (MIN1PIPE) for automatic processing of single-photon calcium imaging data that uses different algorithms for movement correction and signal extraction and outperforms existing methods.

Highlights

- A generic end-to-end processing pipeline (MIN1PIPE) for 1-photon calcium imaging
- A hierarchical motion correction module corrects all types of deformations
- A seeds-cleansed signal extraction module automatically extracts shapes and traces
- MIN1PIPE removes the parameters unknown *a priori* but central in other algorithms



MIN1PIPE: A Miniscope 1-Photon-Based Calcium Imaging Signal Extraction Pipeline

Jinghao Lu,^{1,*} Chunyuan Li,^{3,*} Jonnathan Singh-Alvarado,¹ Zhe Charles Zhou,^{4,5} Flavio Fröhlich,^{4,5} Richard Mooney,¹ and Fan Wang^{1,2,6,*}

¹Department of Neurobiology, Duke University Medical Center, Duke University, Durham, NC 27710, USA

²Department of Cell Biology, Duke University Medical Center, Duke University, Durham, NC 27710, USA

³Department of Electrical and Computer Engineering, Duke University, Durham, NC 27710, USA

⁴Department of Psychiatry, University of North Carolina at Chapel Hill, Chapel Hill, NC 27599, USA

⁵Neurobiology Curriculum, University of North Carolina at Chapel Hill, Chapel Hill, NC 27599, USA

⁶Lead Contact

*Correspondence: jinghao.lu@duke.edu (J.L.), chunyuan.li@duke.edu (C.L.), fan.wang@duke.edu (F.W.)

<https://doi.org/10.1016/j.celrep.2018.05.062>

SUMMARY

In vivo calcium imaging using a 1-photon-based miniscope and a microendoscopic lens enables studies of neural activities in freely behaving animals. However, the high and fluctuating background, the inevitable movements and distortions of imaging field, and the extensive spatial overlaps of fluorescent signals emitted from imaged neurons inherent in this 1-photon imaging method present major challenges for extracting neuronal signals reliably and automatically from the raw imaging data. Here, we develop a unifying algorithm called the miniscope 1-photon imaging pipeline (MIN1PIPE), which contains several stand-alone modules and can handle a wide range of imaging conditions and qualities with minimal parameter tuning and automatically and accurately isolate spatially localized neural signals. We have quantitatively compared MIN1PIPE with other existing partial methods using both synthetic and real datasets obtained from different animal models and show that MIN1PIPE has superior efficiency and precision in analyzing noisy miniscope calcium imaging data.

INTRODUCTION

In vivo calcium imaging of activities from large populations of neurons in awake and behaving animals has become one of the staple technologies in neuroscience (Cai et al., 2016; Flusberg et al., 2008; Ghosh et al., 2011). Recent advances in single-photon-based miniscope technology have further enabled imaging of neural ensemble activities in freely moving animals (Cai et al., 2016; Flusberg et al., 2008; Ghosh et al., 2011), thereby allowing circuits involved in a rich repertoire of animal behaviors to be examined. For example, this technology has been successfully used in probing dynamics of neural circuits involved in innate behaviors (Betley et al., 2015; Douglass et al., 2017; Jennings et al., 2015), decision making (Pinto and Dan, 2015; Carvalho Poyraz et al., 2016), motor control (Klaus

et al., 2017), learning and memory (Grewe et al., 2017; Kamigaki and Dan, 2017; Kitamura et al., 2017; Roberts et al., 2017; Roy et al., 2017; Xu et al., 2016), social memory (Okuyama et al., 2016), hippocampal place coding (Ziv et al., 2013), sleep (Cox et al., 2016; Weber and Dan, 2016), bird song (Markowitz et al., 2015), and pathological processes (Berdycheva et al., 2016).

The increasing popularity of the miniscope calcium imaging technology demands the development of a fully automatic and robust signal-processing method that can reliably extract neuronal signals from the noisy single-photon calcium imaging data. Ideally, the processing method (1) should be able to handle a wide range of imaging conditions (e.g., high fluctuating background) and results with minimal parameter tuning and (2) should have minimal assumptions about the quality of the data, such as being free of movement or distortion, or sufficiently good signal-to-noise ratio (SNR). Existing imaging processing algorithms do not meet these two criteria.

For extraction of neuronal signals, many previous methods work well in situations with high SNR and stable field of views; therefore, they are best suited for processing two-photon imaging data (Apthorpe et al., 2016; Maruyama et al., 2014; Pachitariu et al., 2013; Pnevmatikakis et al., 2016; Reidl et al., 2007). In single-photon miniscope imaging, existing automatic signal extraction methods mainly include principal-component analysis/independent component analysis (PCA/ICA) (Mukamel et al., 2009) and constrained nonnegative matrix factorization-extended (CNMF-E) (Zhou et al., 2018). PCA/ICA (Mukamel et al., 2009) was the first attempt to automatize the signal extraction process from miniscope imaging data using PCA followed by ICA to extract signals from background and involving manual annotations of regions of interest (ROIs). A latest method, CNMF-E, adapts the constraint matrix factorization framework (Zhou et al., 2018). Specifically, because the data from single-photon imaging are dominated by a noisy, uneven, and fluctuating background, CNMF-E uses a sophisticated background fitting model to better characterize the non-neuronal dynamics and is, thereby, better at identifying neuron-like ROIs (Zhou et al., 2018). However, both PCA/ICA and CNMF-E have false-negative and false-positive issues in ROI identification, as we will illustrate in the Results section. Furthermore, these methods depend on sophisticated parameter tuning, especially requiring setting parameters that are unknown *a priori* in practice, such as “number of neurons.”



Another major issue is movements (including distortions) during imaging, which are often inevitable in awake behaving animals. Movements and distortions need to be corrected to allow image frames to be properly aligned before the time-varying neural activity signals can be reliably extracted automatically. Many methods were developed independently in attempt to solve this problem. For example, several approaches register frames through template matching based on the assumption that the major form of movements is translational displacement (Dubbs et al., 2016; Thévenaz et al., 1998). To eliminate such assumptions, methods with block-based displacement field estimation were developed, with image feature matching algorithms extended from the Lucas-Kanade tracker (Greenberg and Kerr, 2009; Lucas and Kanade, 1981) or hidden Markov models (Dombeck et al., 2007; Kaifosh et al., 2013). Some of these movement correction methods have been included as a module in a larger toolbox, using the frame-wise rigid registration approaches (Kaifosh et al., 2014; Pachitariu et al., 2016). A recent approach called NoRMCorre attempts to solve the problem of nonrigid movement correction in a large field of view, but it, too, used a block-based registration (Pnevmatikakis and Giovannucci, 2017). Therefore, all existing methods make specific assumptions about both the form and magnitude of the potential movements when applied to handle nonrigid movement registrations. However, this assumption does not hold true for movements with distortions of the field of view that often happen in single-photon imaging. Furthermore, errors in the movement correction can easily propagate, since these previous methods all register frames based on a single reference frame. Considering that extracting neural activity signals is highly dependent on removing movement artifacts, an accurate and robust movement correction module is imperative.

Here, we develop the miniscope 1-photon imaging signal extraction pipeline (MIN1PIPE) that takes the very raw calcium videos as inputs and automatically removes background while preserving signals, corrects movements with no assumptions of the types of movements, and delivers separated neuronal ROIs as well as deconvolved calcium traces as outputs. The MIN1PIPE contains a neural enhancing module that minimizes the influence of background unevenness and fluctuations, a hierarchical movement correction module that can handle all kinds of deformation with minimal error propagation, and a seeds-cleansed neural signal extraction module that identifies the set of real ROIs and their corresponding calcium traces without setting unknown parameters *a priori* (Figure 1). Though our MIN1PIPE is primarily developed for single-photon-based miniscope imaging, individual modules can also be independently combined with other processing algorithms to improve performance in analyzing two-photon imaging.

RESULTS

Core Modules in MIN1PIPE Neural Enhancing Module

The core of MIN1PIPE relies on turning the imaging data into a stack of background-free, baseline-corrected frames as the first step (Figure 1A). Due to the complex spatiotemporal properties of background dynamics, our method applies a frame-wise

background estimator that is adaptive to the local properties. We took an idea from mathematical morphology and computer vision in that the foreground neural signals can be approximated by subtracting the estimated background in a denoised image. Therefore, we first remove the grainy noise inherent to the single-photon system (see an example of such grainy noise in Figure S1) while preserving the boundary between foreground and background, and this is achieved by applying an anisotropic diffusion denoising operation (Perona and Malik, 1990) on the raw imaging frames. Next, we use a simple straightforward morphological opening operation (Serra and Vincent, 1992) as the background estimator, with the size of the structure element similar to that of the neurons in the imaging field. The opening operation removes structures smaller than the desired structure element. Subsequently, the foreground that contains all the neuronal signals with the minimal noise is computed as the difference between the denoised raw and the morphological opened frames (Figures 1A and S1).

Movement Correction Module

After the neural signals are enhanced, we next correct for movements in the imaging videos (Figure 1B). The problem of movement correction can essentially be broken down to image stack registration. However, without setting specific constraints on the form or magnitude of the movements, even the most efficient registration algorithms require a running time on the order of seconds to minutes per frame (Vercauteren et al., 2009). Considering that the general imaging datasets contain tens of thousands of frames, the time required for applying these sophisticated image registration methods to every frame is inconceivable. Here, we develop a hierarchical video registration framework for the correction of all types of movement without sacrificing the precision or the speed of corrections. Our framework first decomposes the imaging video into two sections: the stable sections, whose movements can be approximated by small translational displacement, and the non-stable sections that contain large general deformation. This step uses the Kanade-Lucas-Tomasi (KLT) tracker that estimates the displacement of potential corner-like features between two neighboring frames (Shi and Tomasi, 1994). Next, we use three levels of different strategies to align images. At the first level, we correct the small translational displacement within each stable section using the fast Lucas-Kanade tracker, which can be performed efficiently in parallel on multiple sections (Lucas and Kanade, 1981). We then incorporate a diffeomorphic Log-Demons image registration method, which can handle large deformations while preserving the local geometrical properties (Vercauteren et al., 2009). At the second level, we align all the stable sections. The overall information of each section is extracted to form a sectional image. We then apply KLT and LogDemons to sectional images in a pairwise manner and calculate the pairwise similarity of the sectional images, which generates a directed graph among all sectional images. The similar sectional images after registration, which form a cluster in the graph, are combined, and the aforementioned iteration is repeated until all sectional images are combined. The estimated displacement field is then applied to each frame within the same stable section. At the third level, we use a similar process to register the individual frames within each non-stable section, which

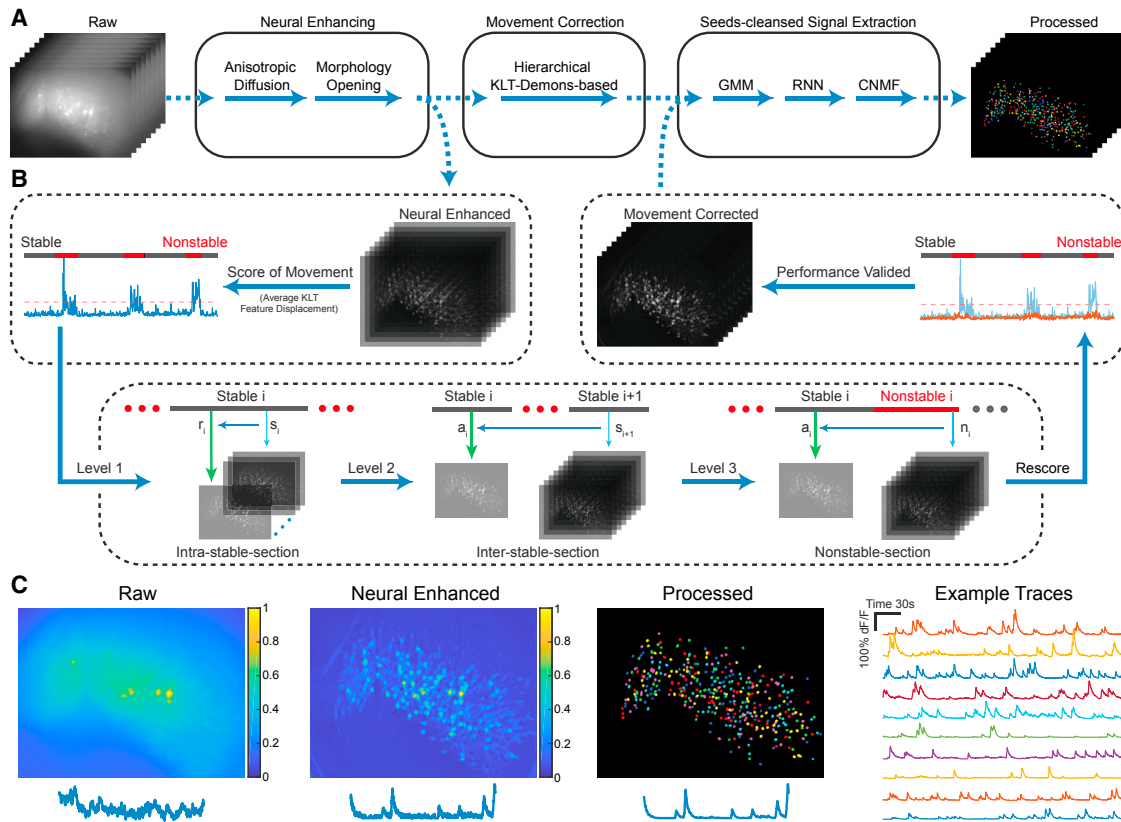


Figure 1. The General Pipeline and Demonstrations of MIN1PIPE

(A) The overall structure of MIN1PIPE. MIN1PIPE takes the very raw miniscope imaging data freshly collected from the imaging system as inputs and returns fully processed ROI components with spatial footprints and temporal calcium traces as outputs. The data are processed in series by neural enhancing, hierarchical movement correction, and seeds-cleansed signal extraction modules. Each module is composed of specific brick functions.

(B) A zoom-in of the hierarchical movement correction module. The module is KLT-Log Demons based. It first scores all the neural enhanced frames and divides them into stable and nonstable sections and then registers frames at three different levels. The movement-corrected frames are then fed into the seeds-cleansed neural signal extraction module.

(C) The demonstrations of MIN1PIPE at key steps. Frames are from the raw imaging video, which contains large, dominant background fluctuation; the neural enhanced video, which contains mainly neural signals; and the fully processed video, which contains only extracted and denoised neural signals as independent ROI components. Rightmost panel: example traces are randomly selected from the processed video.

See also [Figures S1](#) and [S2](#) and [Video S6](#).

can be parallelized to boost performance efficiency (Figure 1B). This hierarchical approach significantly reduces the total registration time due to the balanced assignment of different methods. Importantly, the common registration error does not propagate with this approach.

Seeds-Cleansed Neural Signal Extraction Module

Once movements are corrected and images are aligned, the main task turns to the neural signal extraction. MIN1PIPE extracts neural signals automatically in two main steps (Figure 1C): (1) the seeds-cleansing step to reliably detect the set of real ROIs and (2) a simplified spatiotemporal CNMF to separate ROIs and corresponding calcium traces (Pnevmatikakis et al., 2016). Previous methods contain either no explicit seeds-initialization step or only a coarse initialization that compromises between precision and recall. In contrast, our seeds-cleansing step forces the algorithm to find the set of real ROIs. This is achieved by first generating an over-complete set of seeds containing all potential centers of real ROIs at the cost of including false positives. This

over-complete set is then coarsely cleansed by applying a two-component Gaussian mixture model (GMM) on the peak-valley difference of corresponding traces of the seeds, where the traces of real neurons usually have larger fluctuations compared to the non-neuron false-positive seeds. The GMM removes most background false positives without losing real neurons (Figure S2). To further remove the remaining false positives, such as the ones with abnormal background fluctuations or hemodynamics, we have trained recurrent neural networks (RNNs) with a long-short term memory (LSTM) module offline as the classifier for calcium spikes (Figure S2) (LeCun, Bengio and Hinton, 2015; Hochreiter and Schmidhuber, 1997). Those seeds whose traces contain RNN-identified calcium spikes, regardless of their temporal locations, are classified as true positives, whereas the rest are deemed as false positives. After such cleansing processes, there is still a low possibility of identifying multiple seeds within a single ROI. Therefore, we merge potentially redundant seeds by computing the temporal similarity of seeds within their

neighborhoods and preserving the ones with maximum intensity. With the cleansed set of seeds as the initial position of ROIs, we next perform the iterative spatial and temporal optimizations, as proposed in CNMF, to update the spatial footprints of individual ROIs and the temporal traces with deconvolved spike trains. Notably, unlike previous CNMF or CNMF-E, where the spatial footprints are sequentially updated and subtracted from the preceding residuals, we extract spatial footprints from the original data that do not depend on preceding iterations. Therefore, the information loss and/or duplication is reduced, and the optimization procedures can be parallelized in our method. We show example results obtained using the MIN1PIPE methodology including a raw frame, the fully processed ROIs, and the example traces from ROIs (Figure 1C). The full description of all algorithms used for MIN1PIPE can be found in the [Supplemental Information](#) (see [Detailed Explanation of the Algorithms](#)).

Quantitative Comparisons of the MIN1PIPE Signal Extraction Module with Other Methods

The neural signal extraction and movement correction are two independent problems that can be tested separately. For the signal extraction, we test the performance on synthetic datasets with various signal levels, while for the movement correction, we can directly test it on real data. To measure the performance of the signal extraction, we use a scoring metric that evaluates the spatial and temporal similarity between the ground truth and the identified ROIs and calculate true positives, false positives, and false negatives. To measure the performance of the movement correction, we use a metric based on the average displacement of feature points between neighboring frames (for details, please see [Supplemental Experimental Procedures](#)).

We synthesized 16 imaging videos with signal levels (SLs, defined as the ratio of the amplitude between the signals and the background) ranging from 0.05 to 0.8. Each video contains 3,000 frames, with 100 neurons of various shapes and calcium dynamics, and background fluctuations extracted from real datasets. The properties of synthetic videos resemble those of real data, whose SL falls between the range of 0.2 and 0.8. The condition at an SL of 0.05 is an extreme (Figure S3; Videos S1, S2, and S3). For synthetic datasets, we compare MIN1PIPE with PCA/ICA, CNMF, and CNMF-E for the signal extraction part. For PCA/ICA, we used commercially available Mosaic software (Inscopix), which implements the PCA/ICA method (Mukamel et al., 2009), and processed the data following the standard workflow in the software manual. In particular, we chose the number of principal components (PCs) and independent components (ICs) based on the suggested rate (e.g., 20% more ICs and 50% more PCs than the estimated number of ROIs). For CNMF and CNMF-E, we used online codes with the default initialization strategy in Pnevmatikakis et al. (2016) and Zhou et al. (2018).

The results of ROI detection (Figure 2A) and the calcium traces from one example ROI obtained by different methods (Figure 2B) at SLs of 0.2 and 0.8 are compared. The contours of the identified ROIs using different methods are drawn and superimposed onto the maximum projection of the ground truth. For both SLs, MIN1PIPE can identify the nearly complete set of ROIs (99% and 100% for SLs of 0.2 and 0.8, respectively) with minimal false positives (FPs) (0% FPs in both conditions), whereas the other

methods either detect partial subsets of ROIs (PCA/ICA: 0% at an SL of 0.2 and ~65% true positives at an SL of 0.8; CNMF: ~32% at an SL of 0.2 and ~95% true positives at an SL of 0.8) or include significantly more FPs (CNMF-E: ~20% FPs at an SL of 0.2 and ~5% FPs at an SL of 0.8). In addition, the extracted spatial footprints are less realistic with the PCA/ICA or previous CNMF-based methods. The example calcium traces indicate that MIN1PIPE has a near-optimal performance in extracting individual ROIs, even at low SLs when compared to the ground truth traces (Figure 2B), and even when the background contains synchronous firing (Figure S4). In contrast, PCA/ICA fails to identify ROIs, while CNMF fails to separate neurons from overlapping ROIs when the SL is low. CNMF-E, on the other hand, falsely identified separated components that actually belong to the same ROI in both high and low SL conditions. This could be a serious issue in practice. Figure 2F shows the extracted traces of individual unmerged components using CNMF-E. These components are dissimilar. Because similarity score is a criterion used by the CNMF-E to merge components, CNMF-E fails to recognize that these components actually belong to one single ROI. This is likely due to overfitting the traces of individual seeds by CNMF-E, resulting in the divergence of similarity between the traces of the different patches that belong to the same neuron. Figure 2C summarizes the performance accuracy of these three methods at all SLs. The plots of the true positives show that both MIN1PIPE and CNMF-E are significantly better at extracting correct signals in almost all conditions compared to PCA/ICA and CNMF; while the plots of FPs and false negatives indicate that MIN1PIPE has a significantly superior performance in avoiding false-positive signals and outperforms the other methods in the extreme conditions. The summary plots (Figure 2D; Figure S3) of the spatiotemporal similarities between the extracted results and the ground truth (shown as clouds of dots) reveal, again, that both MIN1PIPE and CNMF-E outperform the other two methods in extracting the “successfully identified” ground-truth signals. However, when we consider both the precision and recall of the signal extraction results by computing the F_1 score (the harmonic average of precision and recall), MIN1PIPE outperforms all the other methods within a broad range of SLs (Figure 2E).

Quantitative Validation of the MIN1PIPE Movement Correction Module

To validate the performance of the movement correction module in MIN1PIPE, we applied the module on video sections with large deformation movements of the imaging field. Specifically, we chose a video obtained through two-photon imaging of the ferret's posterior parietal cortex as an example due to its particularly frequent and large deformations (Video S4, as a demo section of the full video). Figure 3A shows an example of 3 consecutive frames (with each frame pseudo-colored as pink, green, or blue) with large nonlinear deformations between frames superimposed together. The two rigid-transform-based methods (Lucas-Kanade [LK] and KLT Affine) by themselves fail to fully remove the large deformations, whereas MIN1PIPE (combining the Log-Demons registration) succeeds in correcting these movements. We further quantified the performance of correction by calculating the average displacement of feature

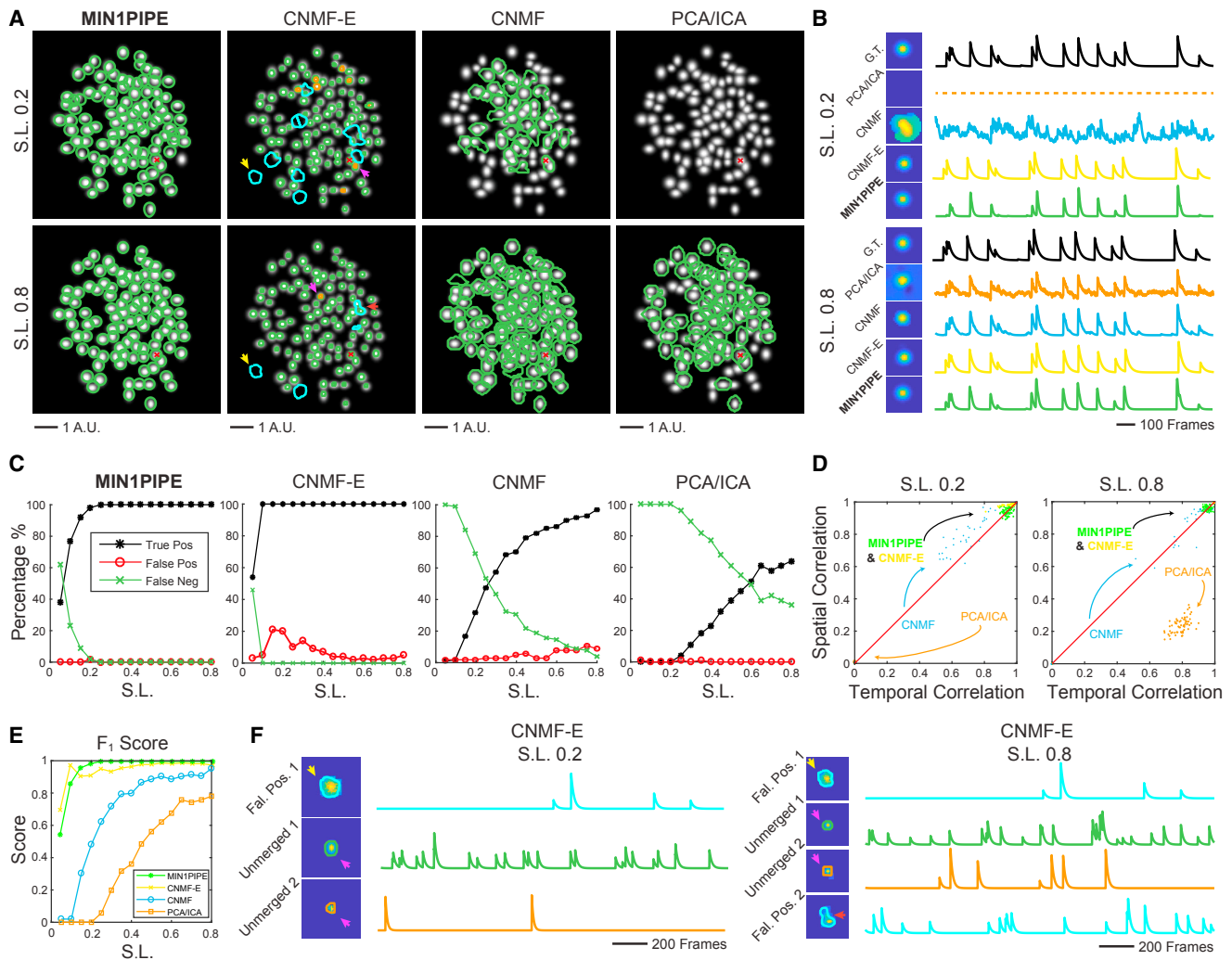


Figure 2. Quantitative Comparisons of the MIN1PIPE Signal Extraction Module with Other Methods on Simulated Datasets

(A) The identified ROI contours of the four methods at two representative S.Ls. Green circles indicate the ROI contours, while the cyan and orange circles show the falsely identified and the unsuccessfully merged ROI components, respectively. S.L., signal level (the ratio of the amplitude between the signals and the background noise); A.U., arbitrary unit.

(B) The trace of an example ROI component (indicated by the red crossing in A) identified by the four methods and the ground truth. G.T., ground truth.

(C) The identification precision and accuracy of the four methods. Note that, although both MIN1PIPE and CNMF-E show more correctly identified ROIs, MIN1PIPE also avoids almost all of the FPs identified by CNMF-E.

(D) The spatiotemporal identification accuracy with the four methods at two representative S.Ls. The similarities of the spatial footprints and temporal traces between the results of the three methods and the ground truth of each ROI are plotted as dots in the figure.

(E) The plot of F₁ score of the four methods, where F₁ score computes the harmonic average of precision and recall. Note that, when considering both the true-positive and false-positive accuracies, MIN1PIPE returns the best outcome among the four methods.

(F) The incorrectly identified components by CNMF-E at two S.Ls, indicated by the arrows in (A). The FPs are seen in both S.Ls (and also ubiquitous across all S.Ls); so are the unmerged components.

See also [Figures S3](#) and [S4](#) and [Videos S1](#), [S2](#), and [S3](#).

points between two neighboring frames before and after the movement correction ([Figure 3B](#)). Before correction, the score of average displacement shows frequent bursts of large deformation periods, whereas after correction, the score of displacement shows a nearly flat line. Notably, the frames with large deformations are all well aligned ([Figure 3B](#), lower panels; [Video S4](#)). We further compare this module with the recently published NoRMCorre ([Pneumatikakis and Giovannucci, 2017](#)) method,

using a demo clip that is not spatially down-sampled and contains large deformations between neighboring frames. [Figure 3C](#) shows the raw and the corrected movement scores: MIN1PIPE successfully reduces the movements to baseline levels, whereas NoRMCorre retains large residuals ([Figure 3C](#)). Using another metric—the correlation with the mean (CM), as proposed in NoRMCorre—MIN1PIPE also clearly outperforms NoRMCorre ([Figure 3D](#)). As an example, we show images of two neighboring

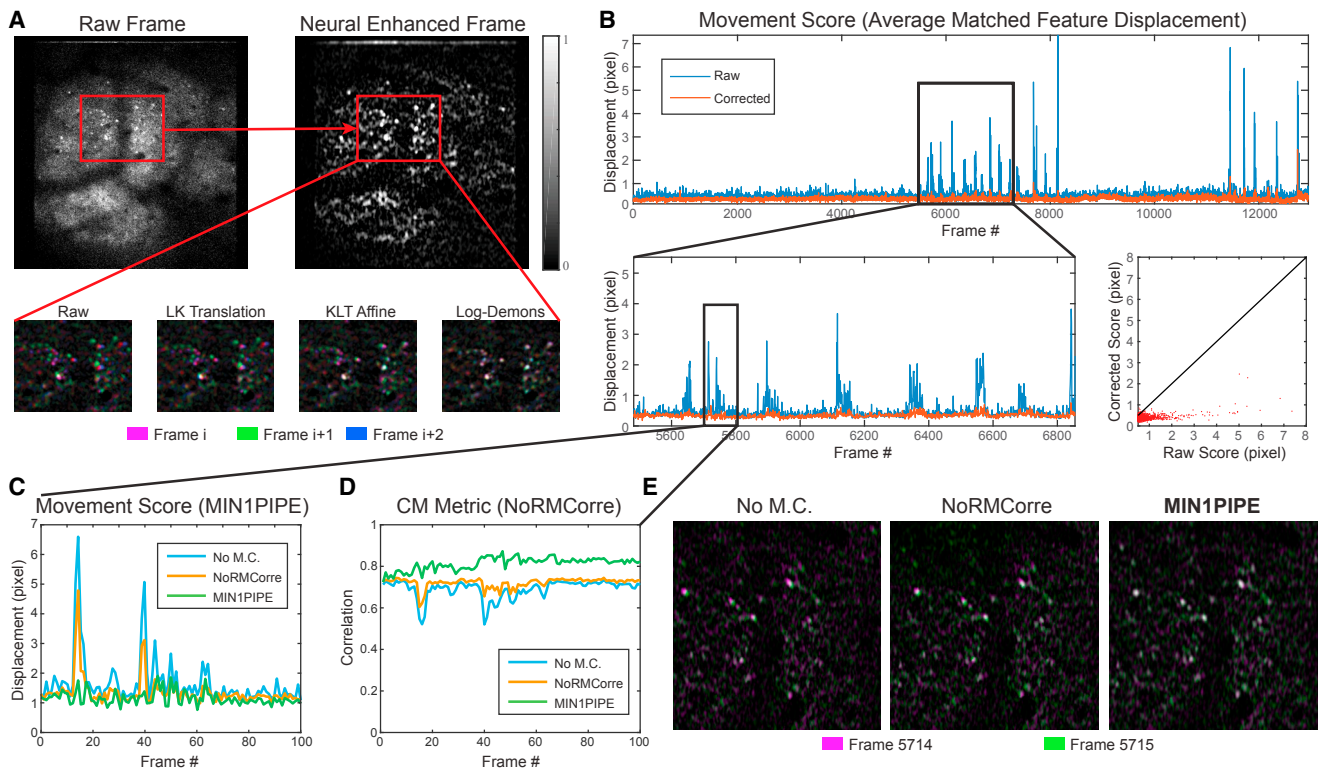


Figure 3. Quantitative Demonstration of the Performance of the Movement Correction Module in MIN1PIPE

(A) The demonstration of various image registration methods in three consecutive frames from two-photon imaging data. The deformation registration algorithm we use in the module (Log-Demons) successfully corrects all the nonrigid deformations within the frames that cannot be corrected by the methods that assume translation or rigid transformation. Black and white indicate the overlap of the same structure between the frames, whereas other colors indicate nonaligned structures.

(B) Upper: the score of movement before and after the correction in the full dataset (spatially down-sampled with ratio of 0.5). Bottom left: a zoom-in at the period with intense movements. Bottom right: the scatterplots of the scores of all frames before and after movement. In general, the hierarchical correction steps register large deformations while preserving the stable frames.

(C) The comparison of the score of movement with NoRMCorre. MIN1PIPE corrects large deformations to baseline levels, while NoRMCorre contains obvious residuals of some frames with large deformations.

(D) The comparison of the CM metric with NoRMCorre. While NoRMCorre elevates the CM score to some degree, deformation residuals are still visible, i.e., the valleys of the score. On the other hand, MIN1PIPE significantly elevates the CM score of all frames.

(E) Example images showing the performance by the two methods. Each image shows the two superimposed neighboring frames that originally contains large deformations and the movement-corrected ones by the two methods.

See also [Video S4](#).

frames (number 5,714 and 5,715 in the full video) superimposed together ([Figure 3E](#)) in raw or movement-corrected conditions using the two methods.

Application of MIN1PIPE on Real Miniscope Imaging Datasets

We next compare the performance of MIN1PIPE with PCA/ICA and CNMF-E methods on real datasets. We first applied the three different methods to miniscope calcium imaging data obtained using prism probes from layers 2 and 3 of the barrel cortex in freely moving mice. GCaMP6f was expressed in layer 2/3 neurons using adeno-associated virus (AAV), and signals were imaged continuously over 5 min when the mouse freely explored its environment. Following the general pipeline of MIN1PIPE ([Supplemental Experimental Procedures](#)), our method removed the strong, uneven background structure and

automatically identified 357 putative ROI components without the need for additional manual selection ([Figure 4A](#); [Video S5](#)). In comparison, PCA/ICA identified 79 ROIs, whereas CNMF-E identified 598 ROIs. The contours of the ROIs identified by the different methods are drawn and superimposed onto the maximum projection of the neural enhanced data ([Figure 4B](#)). This reveals that MIN1PIPE can identify potentially all ROIs, with each containing a single and well-shaped component, whereas PCA/ICA misses a significant subset of ROIs. CNMF-E covers almost all potential ROIs, but this is achieved at the cost of returning many unmerged components (falsely separated ROIs), similarly to what it did on synthetic data. PCA/ICA and CNMF-E also have some problems in separating overlapping ROIs and/or estimating the correct shape of the ROIs, as revealed by the max projections of the extracted signals ([Figure 4C](#)). The projection of MIN1PIPE-extracted signals closely

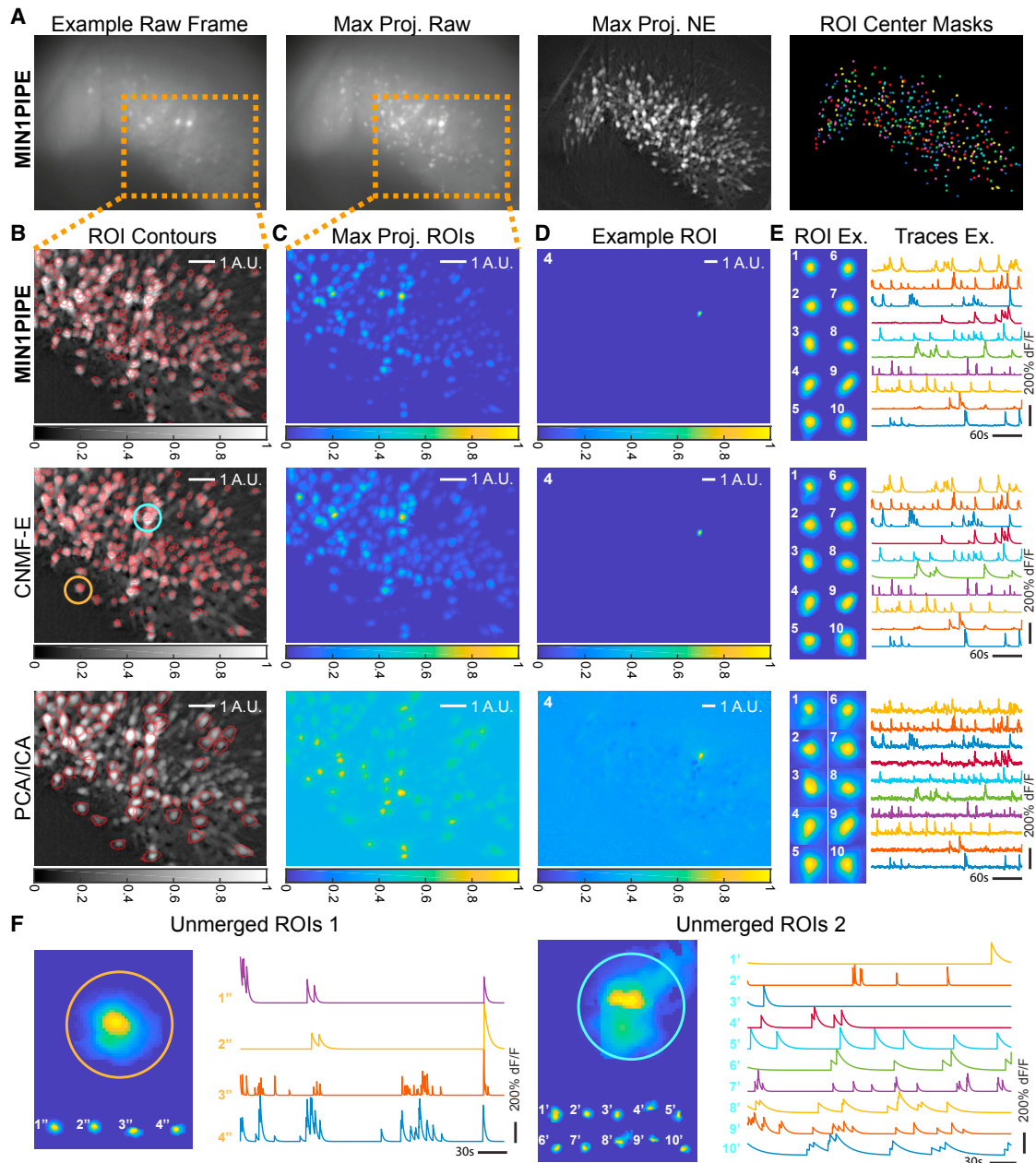


Figure 4. Comparing Different Methods Using Miniscope Imaging Data from the Mouse Barrel Cortex

(A) Demo of MIN1PIPE in processing imaging data from the barrel cortex. We show an example raw frame, the maximum projection of raw video, the maximum projection of the neural enhanced video, and the colored ROI masks.

(B) The identified ROI contours superimposed on the maximum projection of neural enhanced video. MIN1PIPE returns a set of ROIs with well-shaped, localized, spatial footprints. PCA/ICA identifies only a small subset of true positives (79), and the footprints are not localized. CNMF-E captures most ROIs but also many unmerged components from the same ROIs. The projection map is shown as a grayscale colormap.

(C) The maximum projections of all identified ROI footprints. This further demonstrates the general properties of the extracted neural components, where MIN1PIPE returns smooth and localized spatial footprints, CNMF-E returns more diffusive and less smooth ones, and PCA/ICA returns nonlocalized ROIs.

(D) The spatial footprint of an example ROI. MIN1PIPE extracted the most localized component that is close to the real shape shown in the neural enhanced projection, whereas CNMF-E extracted a similar one at first glance, and PCA/ICA detected the unrealistic component as a mix of several other components. The number on the top left corner of each panel indicates the identity of this ROI within the 10 examples in (E).

(E) The temporal traces of ten examples randomly selected from the ROIs that are detected by all three methods.

(F) Two examples of the unmerged ROIs identified by CNMF-E. The larger ROI footprints show the maximum projection of all the unmerged individual patches, while the smaller ones are individual patches identified as independent ROIs. There are 4 and 10 unmerged components in these cases, respectively.

See also [Videos S5](#) and [S6](#).

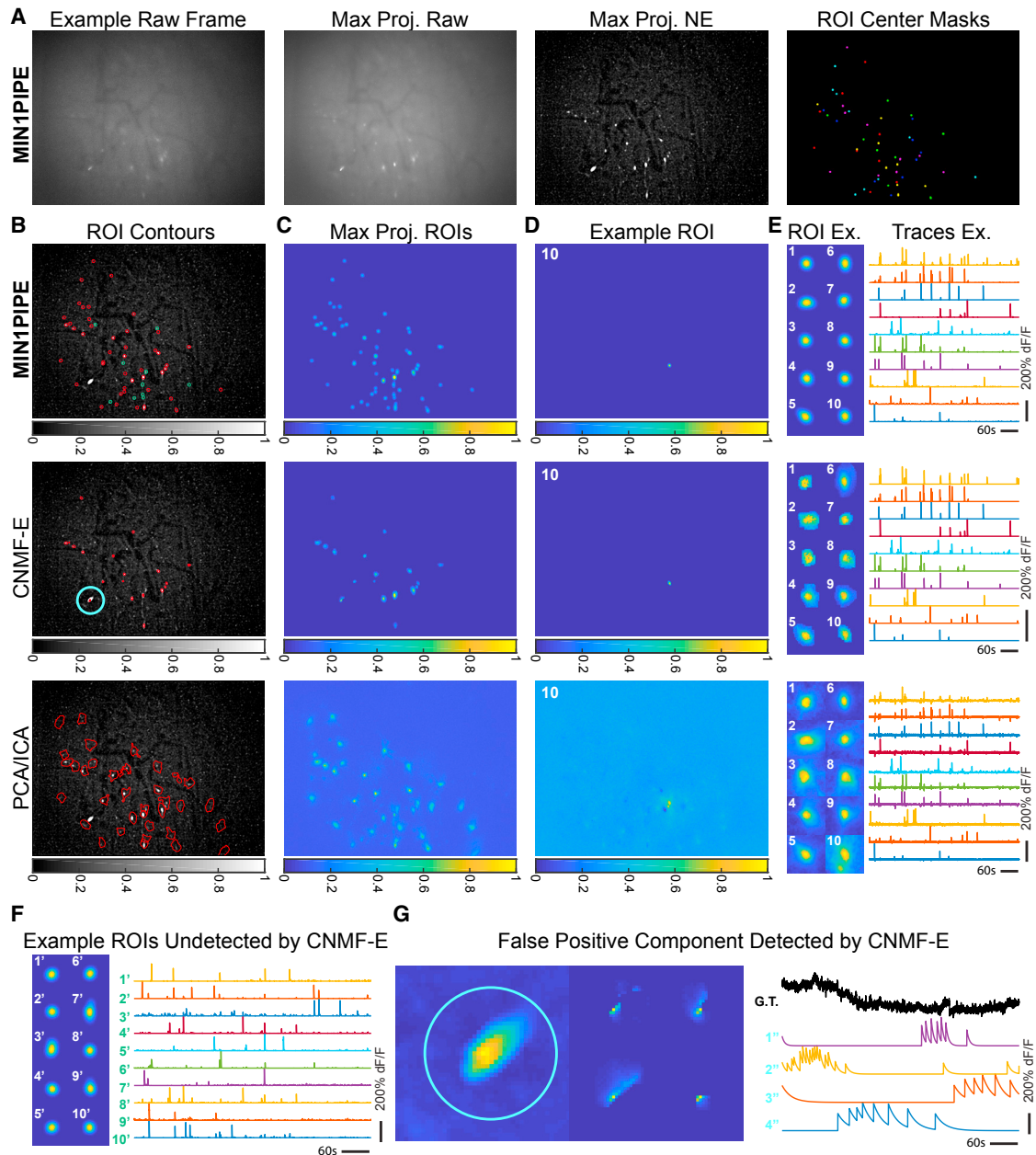


Figure 5. Comparing Different Methods Using Miniscope Imaging Data from the Area X in Zebra Finch

(A) Demo of MIN1PIPE in processing data from Area X in the zebra finch brain. We show an example of the raw frame, the maximum projection of raw video, the maximum projection of the neural enhanced video, and the colored ROI masks.

(B) The identified ROI contours superimposed on the maximum projection of neural enhanced video. MIN1PIPE returns a set of ROIs with well-shaped, localized, spatial footprints. CNMF-E and PCA/ICA identify only a small subset of true positives (22 and 35, respectively), and the footprints either are not localized or are not successfully merged. Besides, there is a clear FP by CNMF-E (indicated with a circle) that also includes several unmerged patches. The projection map is shown as a grayscale colormap.

(C) The maximum projections of all the identified ROI footprints.

(D) The spatial footprint of an example ROI. Note that PCA/ICA extracted an unrealistic component as a mix of several other components.

(E) The spatial footprints and temporal traces of 10 examples selected from the ROIs detected by all three methods. MIN1PIPE extracts localized ROIs close to the real shape. CNMF-E extracts more diffusive and less smooth footprints. PCA/ICA returns nonlocalized ROIs. MIN1PIPE and CNMF-E show the better performance of temporal trace extraction compared with PCA/ICA.

(F) Example ROIs with traces that are identified by MIN1PIPE but not CNMF-E. These are typically the neurons with weak signals, and the extracted footprints and the traces are realistic.

(legend continued on next page)

resembles those of the neural enhanced data (Figure 4C, top). In comparison, the projection obtained using PCA/ICA has low SNR with high background signals (Figure 4C, bottom), while the projection derived from CNMF-E contains blurry and expanded ROI footprints (Figure 4C, middle). To further check the shape of individual ROIs, we choose to visualize one example ROI embedded in the full imaging field using these different methods (Figure 4D) and further selected 10 ROI components that were identified by all three methods within the cropped image field (Figure 4E, individual panels indicated with 1–10). MIN1PIPE delineates well-localized ROI footprints (Figures 4D and 4E, top), whereas CNMF-E returns less smooth ROIs (Figures 4D and 4E, middle). PCA/ICA, on the other hand, fails to provide a localized footprint, as remnants of other ROI components can also be seen (Figures 4D and 4E, bottom). We next plotted the temporal calcium traces extracted by the different methods. Both MIN1PIPE and CNMF-E give denoised traces, whereas the traces obtained using PCA/ICA are noisy and show unrealistic negative fluctuations (Figure 4E, right panels). Furthermore, the traces extracted using CNMF-E tend to have zero background noise, which is good on successfully isolated neurons. However, this operation could leave a large spatiotemporal signal residual in the background after subtracting each identified component. Therefore, later iterations can pick up those residual signals and identify the residual events as new components with incompatibly different traces, hence over-identifying ROIs. Video S6 shows the comparison of raw and processed results using three different methods of the entire imaging video.

To further illustrate the general applicability of MIN1PIPE across brain areas and animal models, we used the method to process calcium imaging data obtained from Area X in the songbird zebra finch and compared the results with those processed using the other two methods. Neurons in Area X are smaller in size than those in mouse barrel cortex, as described earlier (Figure 5A). Briefly, MIN1PIPE detected 55 ROI components, whereas CNMF-E detected 22 and PCA/ICA detected 35 ROIs after manual selection (Figures 5A–5C; Video S7). All of the ROIs detected by CNMF-E and PCA/ICA are included in the set extracted by MIN1PIPE (Figures 5B, 5C, and 5F). Figure 5F shows the footprints and signal traces of a set of ROIs that are false negatives in CNMF-E. Moreover, the PCA/ICA again gives rise to more diffusive and nonlocalized ROI footprints that contain other potential components (Figure 5D, bottom), which results in noisy traces (Figure 5E). CNMF-E again identifies false-positive ROIs due to unmerged components that are apparent upon visual inspections (Figures 5B, 5C, and 5G). For the example shown in Figure 5G, although the real trace shows complete noise structure, CNMF-E overfits each of the components into traces with real calcium spike dynamics, which results in unmerged components and, thus, false-positive ROIs.

It was known that Area X neurons show strong song-selective activities when the bird is singing (Goldberg and Fee, 2010;

Kojima and Doupe, 2007; Woolley et al., 2014; Yazaki-Sugiyama and Mooney, 2004), which can be used as partial ground truth to validate the imaging processing method. We plot the calcium traces of the ROIs identified by MIN1PIPE, and the majority of the ROIs contain calcium events that are roughly phase-locked to the singing onsets (Figure 6A). Notably, a subset of the neurons shows precise singing-related activities with minimal events unrelated to singing (Figure 6B, upper panel). Furthermore, we sorted neurons according to their timing of peak calcium activities during each song production event (Figure 6B, lower panel), and this analysis also reveals a subset of Area X neurons whose activation patterns are closely related to the onset of the singing, consistent with previous findings, and thereby further validates MIN1PIPE.

DISCUSSION

Here, we show that PCA/ICA (Mukamel et al., 2009) has difficulties in delineating localized ROIs and in separating overlapping ROIs for single-photon imaging data. CNMF-E (Zhou et al., 2018) is significantly better at identifying neuron-like ROIs, but it also increases the number of falsely identified ROIs, resulting in numerous unmerged components of the same neurons. This is likely due to overfitting of the neuronal signal dynamics and also leaving residual spatiotemporal signal in the background after subtracting each identified component and subsequent false identification of the residual events as new components. Moreover, both PCA/ICA and CNMF-E rely on the stable imaging field and will fail if the imaging field contains movement.

Compared with existing methods, MIN1PIPE has several key advances. First, MIN1PIPE solves the full range of problems for signal extraction in single-photon miniscope imaging with one pipeline. Specifically, we have developed innovative and robust modules to solve different problems, including: (1) the neural enhancing module that removes the ultra-high and fluctuating background characteristic of single-photon imaging, (2) the hierarchical movement correction module that outperforms existing methods such as NoRMCorre and that is capable of efficiently registering any types of deformations of the imaging field, and (3) the seeds-cleansed neural signal extraction module that utilizes GMM and pretrained RNNs to enable automatic identification and extraction of ROIs and calcium traces. Second, MIN1PIPE eliminates the need for heuristically setting many parameters that not only are unknown *a priori* but also influence the performance of the downstream processing steps, such as setting the number of neurons, a central parameter required by all previous neural signal extraction methods. The importance of this cannot be over-emphasized, because pre-setting unknown parameters can become problematic in practice. For example, overestimating the number of neurons may result in false-positives in identified ROIs before the calcium trace extraction step and also result in the unnecessary consumption of

(G) An example of the FP extracted by CNMF-E. The larger footprint shows the maximum projection of the neural enhanced non-neuron signal, while the four small ones are the extracted “ROI” components. On the right, we show the ground truth (G.T.) trace of this non-neuron signal, and the four “identified” traces by CNMF-E. Simply looking at the traces, one can hardly differentiate those from real calcium signals. See also Video S7.

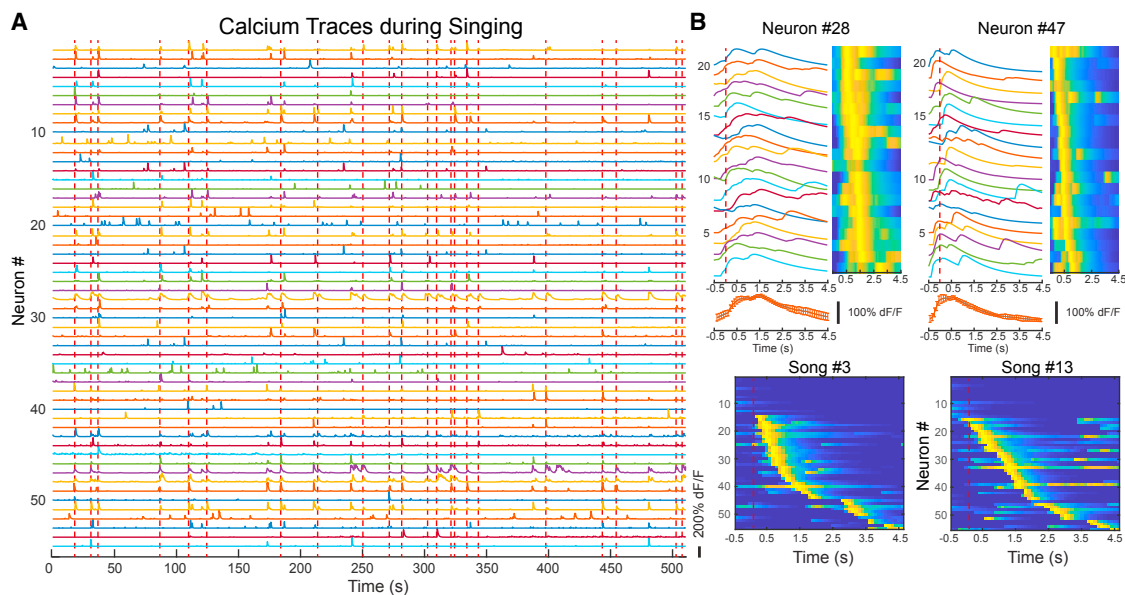


Figure 6. Analysis of Neural Correlation in Area X of Zebra Finch to Singing Behavior

(A) The traces of all automatically detected ROIs with MIN1PIPE superimposed with complete singing onsets in red dashed lines. Note that incomplete song events are not labeled and taken into analysis.

(B) Upper panel: two example neurons with precise song selectivity. The traces represent the neuronal activity of the first 20 complete song singing events, with a window of 0.5 s before and 4.5 s after the song onset. The heatmap is another way of visualizing the analysis. The error bar graphs at the bottom indicate the trial average traces of the two neurons. Lower panel: population activity pattern of two example song-singing events. The neurons are sorted to the latency of the peak. Red dashed lines indicate the onset of songs.

See also [Video S7](#).

computing time. These FPs can only be removed with laborious manual selection without a robust seeds-cleansing step. On the other hand, underestimating the number of neurons will likely lead to false negatives that can never be identified by the downstream steps. Therefore, tweaking this parameter is inevitable in practice using previous methods. While we do not claim that MIN1PIPE completely eliminates the need for manually pruning identified ROIs, our method, indeed, only involves minimal manual interference. Third, MIN1PIPE contains a minimal set of parameters that are easy to interpret and error-tolerant ([Supplemental Information](#)). These include a set of simplified and fixed parameters applicable to various conditions of the popular miniscope platforms (e.g., Inscopix nVista, UCLA open-source miniscope) in our brick algorithm. In addition, all modules use definitive criteria independent of various imaging datasets, which ensures the robustness that the previous combination of setting the number of neurons and the serial initialization procedure could not provide.

In summary, MIN1PIPE provides a generally applicable high-performance toolbox with the modular framework to handle and process 1-photon miniscope imaging data. Interesting future works may integrate more advanced methods to further improve the precision, such as stricter choices of the kernel of anisotropic diffusion ([Chen et al., 2011](#); [Tsotsios and Petrou, 2013](#)), considering spectral invariants to handle very large deformations during non-rigid registration ([Lombaert et al., 2014](#)), using more biologically valid calcium dynamics deconvolution methods ([Speiser et al., 2017](#)), and cross-day registration

methods ([Sheintuch et al., 2017](#)). Additionally, a more robust RNN classifier for seeds cleansing can be trained with more available datasets.

EXPERIMENTAL PROCEDURES

All animal procedures were performed in compliance with the NIH Guide for the Care and Use of Laboratory Animals and approved by the Institute of Animal Use and Care of Duke University and the University of North Carolina at Chapel Hill. Synthetic data for quantitative comparisons with other methods were simulated using increasing levels of background dynamics drawn from a real dataset. Data for movement correction were collected from ferret posterior parietal cortex using two-photon microscopy (NeuroLabware). Real *in vivo* miniscope calcium imaging data for comparison of different methods were collected from mouse barrel cortex and zebra finch Area X using nVista (Inscopix). A detailed description of algorithms and experimental procedures is provided in the [Supplemental Information](#).

Data Analysis

All similarity measures in the main figures were cosine similarity.

SUPPLEMENTAL INFORMATION

Supplemental Information includes Supplemental Experimental Procedures, four figures, and seven videos can be found with this article online at <https://doi.org/10.1016/j.celrep.2018.05.062>.

ACKNOWLEDGMENTS

The MIN1PIPE toolbox, implemented in MATLAB, can be found at the MIN1PIPE repository on GitHub (<https://github.com/JinghaoLu/MIN1PIPE>).

We thank the members of the Wang lab and Mooney lab at Duke University for suggestions and comments. The study is supported by NIH grants DP1-MH103908, R21NS101441, and NS077986 to F.W. and 1R01-NS-099288 to R.M. and by NSF grant IOS-1354962 to R.M.

AUTHOR CONTRIBUTIONS

J.L. and F.W. conceived and designed the project; J.L. designed and implemented all modules of MIN1PIPE; C.L. designed the RNN classifier; J.L. generated the synthetic data; J.L., F.W., J.S.-A., R.M., Z.C.Z., and F.F. designed and/or conducted in vivo imaging experiments; J.L. and C.L. analyzed the data; and J.L., C.L., and F.W. wrote the manuscript.

DECLARATION OF INTERESTS

The authors declare no competing interests.

Received: January 4, 2018

Revised: April 18, 2018

Accepted: May 17, 2018

Published: June 19, 2018

REFERENCES

- Apthorpe, N., Riordan, A., Aguilar, R., Homann, J., Gu, Y., Tank, D., and Seung, H.S. (2016). Automatic neuron detection in calcium imaging data using convolutional networks. In *Advances in Neural Information Processing Systems 29* (NIPS 2016), D.D. Lee, M. Sugiyama, U.V. Luxburg, I. Guyon, and R. Garnett, eds. (Neural Information Processing Systems Foundation), pp. 3270–3278.
- Berdyeva, T.K., Frady, E.P., Nassi, J.J., Aluisio, L., Cherkas, Y., Otte, S., Wyatt, R.M., Dugovic, C., Ghosh, K.K., Schnitzer, M.J., et al. (2016). Direct imaging of hippocampal epileptiform calcium motifs following kainic acid administration in freely behaving mice. *Front. Neurosci.* *10*, 53.
- Betley, J.N., Xu, S., Cao, Z.F.H., Gong, R., Magnus, C.J., Yu, Y., and Sternson, S.M. (2015). Neurons for hunger and thirst transmit a negative-valence teaching signal. *Nature* *521*, 180–185.
- Cai, D.J., Aharoni, D., Shuman, T., Shobe, J., Biane, J., Song, W., Wei, B., Veshkini, M., La-Vu, M., Lou, J., et al. (2016). A shared neural ensemble links distinct contextual memories encoded close in time. *Nature* *534*, 115–118.
- Carvalho Poyraz, F., Holzner, E., Bailey, M.R., Meszaros, J., Kenney, L., Kheirbek, M.A., Balsam, P.D., and Kellendonk, C. (2016). Decreasing striatopallidal pathway function enhances motivation by energizing the initiation of goal-directed action. *J. Neurosci.* *36*, 5988–6001.
- Chen, D., MacLachlan, S., and Kilmer, M. (2011). Iterative parameter-choice and multigrid methods for anisotropic diffusion denoising. *SIAM J. Sci. Comput.* *33*, 2972–2994.
- Cox, J., Pinto, L., and Dan, Y. (2016). Calcium imaging of sleep-wake related neuronal activity in the dorsal pons. *Nat. Commun.* *7*, 10763.
- Dombeck, D.A., Khabbaz, A.N., Collman, F., Adelman, T.L., and Tank, D.W. (2007). Imaging large-scale neural activity with cellular resolution in awake, mobile mice. *Neuron* *56*, 43–57.
- Douglass, A.M., Kucukdereli, H., Ponsérre, M., Markovic, M., Gründemann, J., Strobel, C., Alcalá Morales, P.L., Conzelmann, K.K., Lüthi, A., and Klein, R. (2017). Central amygdala circuits modulate food consumption through a positive-valence mechanism. *Nat. Neurosci.* *20*, 1384–1394.
- Dubbs, A., Guevara, J., and Yuste, R. (2016). moco: Fast motion correction for calcium imaging. *Front. Neuroinform.* *10*, 6.
- Flusberg, B.A., Nimmerjahn, A., Cocker, E.D., Mukamel, E.A., Barretto, R.P., Ko, T.H., Burns, L.D., Jung, J.C., and Schnitzer, M.J. (2008). High-speed, miniaturized fluorescence microscopy in freely moving mice. *Nat. Methods* *5*, 935–938.
- Ghosh, K.K., Burns, L.D., Cocker, E.D., Nimmerjahn, A., Ziv, Y., Gamal, A.E., and Schnitzer, M.J. (2011). Miniaturized integration of a fluorescence microscope. *Nat. Methods* *8*, 871–878.
- Goldberg, J.H., and Fee, M.S. (2010). Singing-related neural activity distinguishes four classes of putative striatal neurons in the songbird basal ganglia. *J. Neurophysiol.* *103*, 2002–2014.
- Greenberg, D.S., and Kerr, J.N. (2009). Automated correction of fast motion artifacts for two-photon imaging of awake animals. *J. Neurosci. Methods* *176*, 1–15.
- Grewe, B.F., Gründemann, J., Kitch, L.J., Lecoq, J.A., Parker, J.G., Marshall, J.D., Larkin, M.C., Jercog, P.E., Grenier, F., Li, J.Z., et al. (2017). Neural ensemble dynamics underlying a long-term associative memory. *Nature* *543*, 670–675.
- Hochreiter, S., and Schmidhuber, J. (1997). Long short-term memory. *Neural Comput.* *9*, 1735–1780.
- Jennings, J.H., Ung, R.L., Resendez, S.L., Stamatakis, A.M., Taylor, J.G., Huang, J., Veleta, K., Kantak, P.A., Aita, M., Shilling-Scriver, K., et al. (2015). Visualizing hypothalamic network dynamics for appetitive and consummatory behaviors. *Cell* *160*, 516–527.
- Kaifosh, P., Lovett-Barron, M., Turi, G.F., Reardon, T.R., and Losonczy, A. (2013). Septo-hippocampal GABAergic signaling across multiple modalities in awake mice. *Nat. Neurosci.* *16*, 1182–1184.
- Kaifosh, P., Zaremba, J.D., Danielson, N.B., and Losonczy, A. (2014). SIMA: Python software for analysis of dynamic fluorescence imaging data. *Front. Neuroinform.* *8*, 80.
- Kamigaki, T., and Dan, Y. (2017). Delay activity of specific prefrontal interneuron subtypes modulates memory-guided behavior. *Nat. Neurosci.* *20*, 854–863.
- Kitamura, T., Ogawa, S.K., Roy, D.S., Okuyama, T., Morrissey, M.D., Smith, L.M., Redondo, R.L., and Tonegawa, S. (2017). Engrams and circuits crucial for systems consolidation of a memory. *Science* *356*, 73–78.
- Klaus, A., Martins, G.J., Paixao, V.B., Zhou, P., Paninski, L., and Costa, R.M. (2017). The spatiotemporal organization of the striatum encodes action space. *Neuron* *95*, 1171–1180.e7.
- Kojima, S., and Doupe, A.J. (2007). Song selectivity in the pallidum-basal ganglia song circuit of zebra finches raised without tutor song exposure. *J. Neurophysiol.* *98*, 2099–2109.
- LeCun, Y., Bengio, Y., and Hinton, G. (2015). Deep learning. *Nature* *521*, 436–444.
- Lombaert, H., Grady, L., Pennec, X., Ayache, N., and Cheriet, F. (2014). Spectral log-demons: diffeomorphic image registration with very large deformations. *Int. J. Comput. Vis.* *107*, 254–271.
- Lucas, B.D., and Kanade, T. (1981). An iterative image registration technique with an application to stereo vision. In *Proceedings of the 7th International Joint Conference on Artificial Intelligence* (Morgan Kaufmann Publishers), pp. 674–679.
- Markowitz, J.E., Liberti, W.A., 3rd, Guitchoyants, G., Velho, T., Lois, C., and Gardner, T.J. (2015). Mesoscopic patterns of neural activity support songbird cortical sequences. *PLoS Biol.* *13*, e1002158.
- Maruyama, R., Maeda, K., Moroda, H., Kato, I., Inoue, M., Miyakawa, H., and Aonishi, T. (2014). Detecting cells using non-negative matrix factorization on calcium imaging data. *Neural Netw.* *55*, 11–19.
- Mukamel, E.A., Nimmerjahn, A., and Schnitzer, M.J. (2009). Automated analysis of cellular signals from large-scale calcium imaging data. *Neuron* *63*, 747–760.
- Okuyama, T., Kitamura, T., Roy, D.S., Itohara, S., and Tonegawa, S. (2016). Ventral CA1 neurons store social memory. *Science* *353*, 1536–1541.
- Pachitariu, M., Packer, A.M., Pettit, N., Dalgleish, H., Hausser, M., and Sahani, M. (2013). Extracting regions of interest from biological images with convolutional sparse block coding. In *Advances in Neural Information Processing Systems 26* (NIPS 2013), C.J.C. Burges, L. Bottou, M. Welling, Z. Ghahramani, and K.Q. Weinberger, eds. (Neural Information Processing Systems Foundation), pp. 1745–1753.
- Pachitariu, M., Stringer, C., Dipoppa, M., Schröder, S., Rossi, L.F., Dalgleish, H., Carandini, M., and Harris, K.D. (2016). Suite2p: beyond 10,000 neurons

- with standard two-photon microscopy. *bioRxiv*. <https://doi.org/10.1101/061507>.
- Perona, P., and Malik, J. (1990). Scale-space and edge detection using anisotropic diffusion. *IEEE Trans. Pattern Anal. Mach. Intell.* *12*, 629–639.
- Pinto, L., and Dan, Y. (2015). Cell-type-specific activity in prefrontal cortex during goal-directed behavior. *Neuron* *87*, 437–450.
- Pnevmatikakis, E.A., and Giovannucci, A. (2017). NoRMCorre: an online algorithm for piecewise rigid motion correction of calcium imaging data. *J. Neurosci. Methods* *291*, 83–94.
- Pnevmatikakis, E.A., Soudry, D., Gao, Y., Machado, T.A., Merel, J., Pfau, D., Reardon, T., Mu, Y., Lacefield, C., Yang, W., et al. (2016). Simultaneous denoising, deconvolution, and demixing of calcium imaging data. *Neuron* *89*, 285–299.
- Reidl, J., Starke, J., Omer, D.B., Grinvald, A., and Spors, H. (2007). Independent component analysis of high-resolution imaging data identifies distinct functional domains. *NeuroImage* *34*, 94–108.
- Roberts, T.F., Hisey, E., Tanaka, M., Kearney, M.G., Chatree, G., Yang, C.F., Shah, N.M., and Mooney, R. (2017). Identification of a motor-to-auditory pathway important for vocal learning. *Nat. Neurosci.* *20*, 978–986.
- Roy, D.S., Kitamura, T., Okuyama, T., Ogawa, S.K., Sun, C., Obata, Y., Yoshiki, A., and Tonegawa, S. (2017). Distinct neural circuits for the formation and retrieval of episodic memories. *Cell* *170*, 1000–1012.e19.
- Serra, J., and Vincent, L. (1992). An overview of morphological filtering. *IEEE Trans. Circuits, Systems & Signal Processing* *11*, 47–108.
- Sheintuch, L., Rubin, A., Brande-Eilat, N., Geva, N., Sadeh, N., Pinchasof, O., and Ziv, Y. (2017). Tracking the same neurons across multiple days in Ca^{2+} imaging data. *Cell Rep.* *21*, 1102–1115.
- Shi, J., and Tomasi, C. (1994). Good features to track. In 1994 Proceedings of IEEE Conference on Computer Vision and Pattern Recognition (IEEE Computer Society Press), pp. 593–600.
- Speiser, A., Yan, J., Archer, E.W., Buesing, L., Turaga, S.C., and Macke, J.H. (2017). Fast amortized inference of neural activity from calcium imaging data with variational autoencoders. In *Advances in Neural Information Processing Systems 30 (NIPS 2017)*, I. Guyon, U.V. Luxburg, S. Bengio, H. Wallach, R. Fergus, S. Vishwanathan, and R. Garnett, eds. (Neural Information Processing Systems Foundation), pp. 4027–4037.
- Thévenaz, P., Ruttimann, U.E., and Unser, M. (1998). A pyramid approach to subpixel registration based on intensity. *IEEE Trans. Image Process.* *7*, 27–41.
- Tsiotsios, C., and Petrou, M. (2013). On the choice of the parameters for anisotropic diffusion in image processing. *Pattern Recognit.* *46*, 1369–1381.
- Vercauteren, T., Pennec, X., Perchant, A., and Ayache, N. (2009). Diffeomorphic demons: efficient non-parametric image registration. *NeuroImage* *45* (1, Suppl.), S61–S72.
- Weber, F., and Dan, Y. (2016). Circuit-based interrogation of sleep control. *Nature* *538*, 51–59.
- Woolley, S.C., Rajan, R., Joshua, M., and Doupe, A.J. (2014). Emergence of context-dependent variability across a basal ganglia network. *Neuron* *82*, 208–223.
- Xu, C., Krabbe, S., Gründemann, J., Botta, P., Fadok, J.P., Osakada, F., Saur, D., Grewe, B.F., Schnitzer, M.J., Callaway, E.M., and Lüthi, A. (2016). Distinct hippocampal pathways mediate dissociable roles of context in memory retrieval. *Cell* *167*, 961–972.e16.
- Yazaki-Sugiyama, Y., and Mooney, R. (2004). Sequential learning from multiple tutors and serial retuning of auditory neurons in a brain area important to birdsong learning. *J. Neurophysiol.* *92*, 2771–2788.
- Zhou, P., Resendez, S.L., Rodriguez-Romaguera, J., Jimenez, J.C., Neufeld, S.Q., Giovannucci, A., Friedrich, J., Pnevmatikakis, E.A., Stuber, G.D., Hen, R., et al. (2018). Efficient and accurate extraction of in vivo calcium signals from microendoscopic video data. *eLife* *7*, e28728.
- Ziv, Y., Burns, L.D., Cocker, E.D., Hamel, E.O., Ghosh, K.K., Kitch, L.J., El Gammal, A., and Schnitzer, M.J. (2013). Long-term dynamics of CA1 hippocampal place codes. *Nat. Neurosci.* *16*, 264–266.